ELSEVIER

Physics of the Earth and Planetary Interiors 123 (2001) 185–204

PHYSICS OF THE EARTH AND PLANETARY INTERIORS

www.elsevier.com/locate/pepi

New constraints on the arctic crust and uppermost mantle: surface wave group velocities, P_n, and S_n

A.L. Levshin*, M.H. Ritzwoller, M.P. Barmin, A. Villaseñor, C.A. Padgett

Department of Physics, Center for Imaging the Earth's Interior, University of Colorado at Boulder, Boulder, CO 80309-0390, USA

Abstract

We present the results of a study of surface wave dispersion across the Arctic region (>60°N) and compare the estimating group velocity maps with new maps of the body wave phases P_n and S_n. Data recorded at about 250 broadband digital stations from several global and regional networks were used to obtain Rayleigh and Love wave group velocity measurements following more than 1100 events with magnitudes $M_s > 5.0$ that occurred in the northern hemisphere from 1977 to 1998. These measurements were used to construct both isotropic and 2Ψ azimuthally anisotropic group velocity maps from 15 to 200 s period. As elsewhere in the world, the observed maps display the signatures of sedimentary and oceanic basins, crustal thickness variations, and upper mantle anomalies under both continents and oceans. We also present P_n and S_n maps produced from a groomed data set of travel times from the ISC and NEIC bulletins. The long period group velocity maps correlate well with P_n and S_n velocities. Finally, at long wavelengths, the estimated 2Ψ azimuthal anisotropy in Rayleigh wave group velocity correlates well with the azimuthal anisotropy in phase velocity obtained in a global scale study of Trampert and Woodhouse. Because attempts to improve the resolution to regional scales change both the amplitude and the pattern of the inferred azimuthal anisotropy, caution should be exercised in interpreting the anisotropy maps.

Keywords: Arctic; Surface waves; Seismic tomography; Crust; Upper mantle

1. Introduction

There have been significant recent advances in a number of Arctic solid earth geophysical disciplines using a variety of observing platforms (ocean subsurface, ocean surface, airborne, satellite) and methodologies (e.g. sea floor topography, gravity and magnetic anomalies, marine drilling, improved coverage of seismic refraction and multi-channel reflection surveys in both oceanic and continental areas). (Johnson and Brass, 1998 provide a recent review of a subset of these developments.) Nevertheless, as a whole, the Arctic solid earth remains among the most poorly characterized and understood regions of the Earth. In particular, it is probably fair to say that large-scale natural-source seismology has provided little insight into the structure or tectonic history of the Arctic. By the 'Arctic', we refer to regions above about 60°N latitude, including both the oceanic and the continental regions, and tacitly mean the crust and uppermost mantle. Some of the principal physiographic features of this region are shown in Fig. 1.

The historical shortage of seismic stations and the inhomogeneous distribution of earthquakes in high northern latitudes has limited the ability of large-scale natural-source seismology to reveal significant information about the Arctic solid earth. Body wave receiver functions and shear wave splitting studies would provide valuable information near the few

* Corresponding author. Fax: +1-303-492-7935.
E-mail address: levshin@colorado.edu (A.L. Levshin).

0031-9201/01/$ – see front matter
PII: S0031-9201(00)00209-0

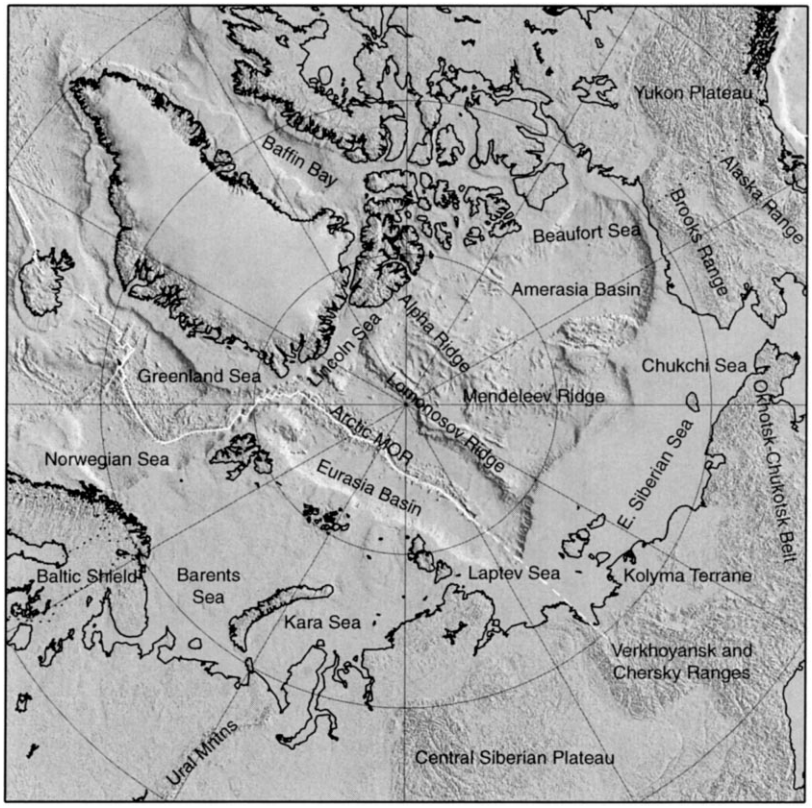

Fig. 1. Major physiographic features above 60°N latitude.

seismic stations that have existed across the Arctic historically, and, as shown later, coverage produced by the uppermost mantle turning phases P_n and S_n is somewhat patchy. Because of the station and earthquake distribution at high northern latitudes, the structure of the Arctic crust and uppermost mantle is best explored with surface waves. Until recently, however, constraints on the Arctic solid earth have come largely from global scale studies which have not been designed to provide optimal coverage or resolution in high latitude regions (e.g. Montagner and Tanimoto, 1991; Trampert and Woodhouse, 1995; Ekström et al., 1997; Masters et al., 1996; Van der Hilst et al., 1997; Bijwaard et al., 1998). In addition, surface wave studies dedicated to the Arctic were completed before the installation of the large number of stations at high northern latitudes that occurred during 1990s. For example, in the study of Zeng et al. (1989) fewer than 100 surface wave paths were available. Other surface wave studies that took place in the late 1970s and 1980s were also severely limited in number of available paths and concentrated on a few widely separated regions, e.g. the Barents Sea shelf (Calcagnille and Panza, 1978; Levshin and Berteussen, 1979; Kijko and Mitchell, 1983; Chan and Mitchell, 1985, 1986; Egorkin et al., 1988), the Laptev Sea shelf (Lander et al., 1985; Lander, 1989), and northern Canada (Chan and Mitchell, 1986).

Therefore, seismic models at high northern latitudes continue to display poorer resolution than elsewhere on the globe. Our goal is to begin to address this situation by providing reliable information for building a significantly improved seismic model of the Arctic crust and uppermost mantle. The information reported here includes new Rayleigh and Love wave group velocity maps and maps of the regional body wave phases P_n and S_n. These maps provide information similar to that produced by Arctic satellite gravity

(e.g. Sobczak et al., 1990) and magnetic maps (e.g. Coles and Taylor, 1990), although at a higher resolution, by providing a large-scale context in which to place smaller scale studies.

This paper summarizes the current state of the continually improving maps of surface wave dispersion, P_n, and S_n across the Arctic. Although still emerging, the current results demonstrate much better spatial resolution than preceding seismological studies of the area. The observed maps clearly display the signatures of sedimentary and oceanic basins, crustal thickness variations, and upper mantle anomalies under both continents and oceans. This study is on-going, and future efforts will improve data coverage significantly. The construction of a 3-D shear velocity model of the crust and uppermost mantle is a natural use of the data presented here.

2. Data selection and processing

To estimate Rayleigh and Love wave group velocities, we used data obtained from about 250 broadband digital stations from a number of global and regional networks, including GSN, GEOSCOPE, USNSN, GEOPHONE, CNSN, MEDNET, KNET, and KAZNET. Data from PASSCAL deployments in Saudi Arabia and Tibet were also used. Seismograms following about 1100 earthquakes with magnitude $M_S \geq 5.0$ that occurred in the northern hemisphere from 1977 to 1998 were selected for processing. Station and earthquake locations are shown in Fig. 2. These data were processed using the frequency–time analysis method described in detail by Levshin et al. (1992) and Ritzwoller and Levshin (1998).

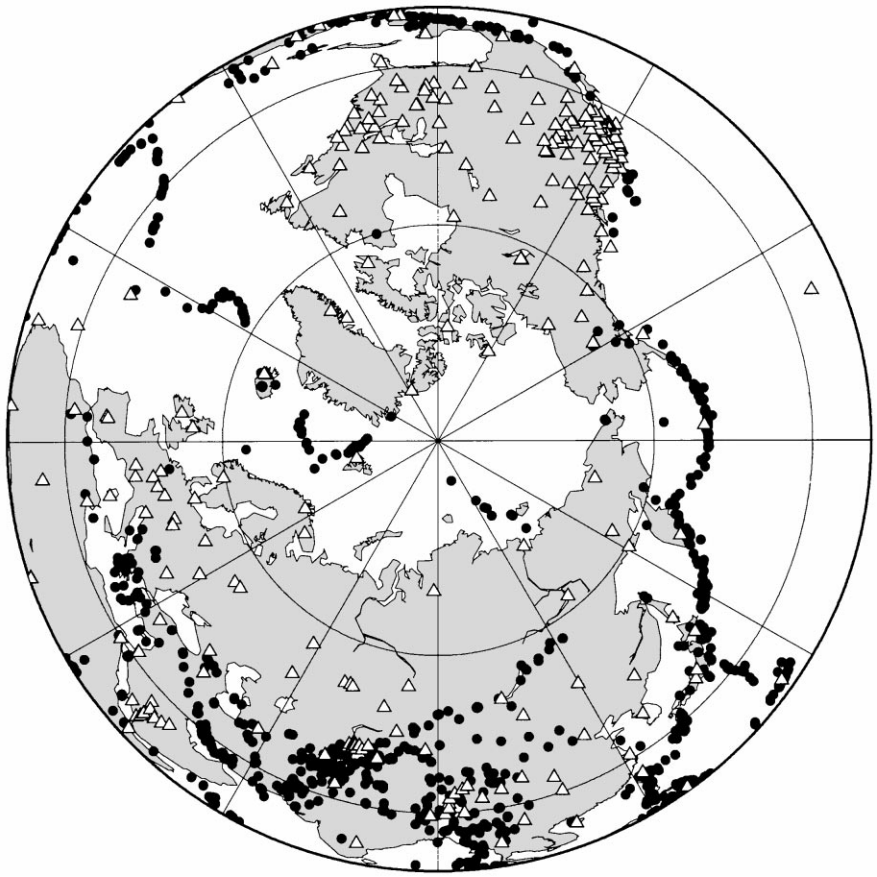

Fig. 2. Location of the 250 stations (triangles) and 1100 events (dots) used in this study.

The measurements used to estimate group velocity maps are chosen rather carefully in an iterative multi-part process. First, at each period and wave type, group travel times are computed using a smoothed global map obtained from the hybrid model composed of the crustal model CRUST5.1 of Mooney et al. (1998) and the mantle model S16B30 of Masters et al. (1996). Measurements that fit the predictions from this model better than three times the overall RMS misfit are retained. Second, these measurements are clustered into summary rays that sample nearly identical 'unique' paths. Third, we use these clustered measurements to estimate very smooth group velocity maps. Finally, the process is restarted from the beginning with the initial data set, measurements are rejected with the estimated smooth maps, and the remaining measurements are reclustered. The resulting data set is what we use to estimate the group velocity maps discussed in the following sections.

The number of unique paths depends on period and wave type. Path numbers maximize near 40 s period and decrease at both shorter and longer periods. Thus, there are about 11,000 unique Rayleigh wave paths at 40 s period across the region of study, but only about 1500 at 15 s and 6000 at 150 s period. The corresponding numbers for Love waves are 7500, 900 and 6000.

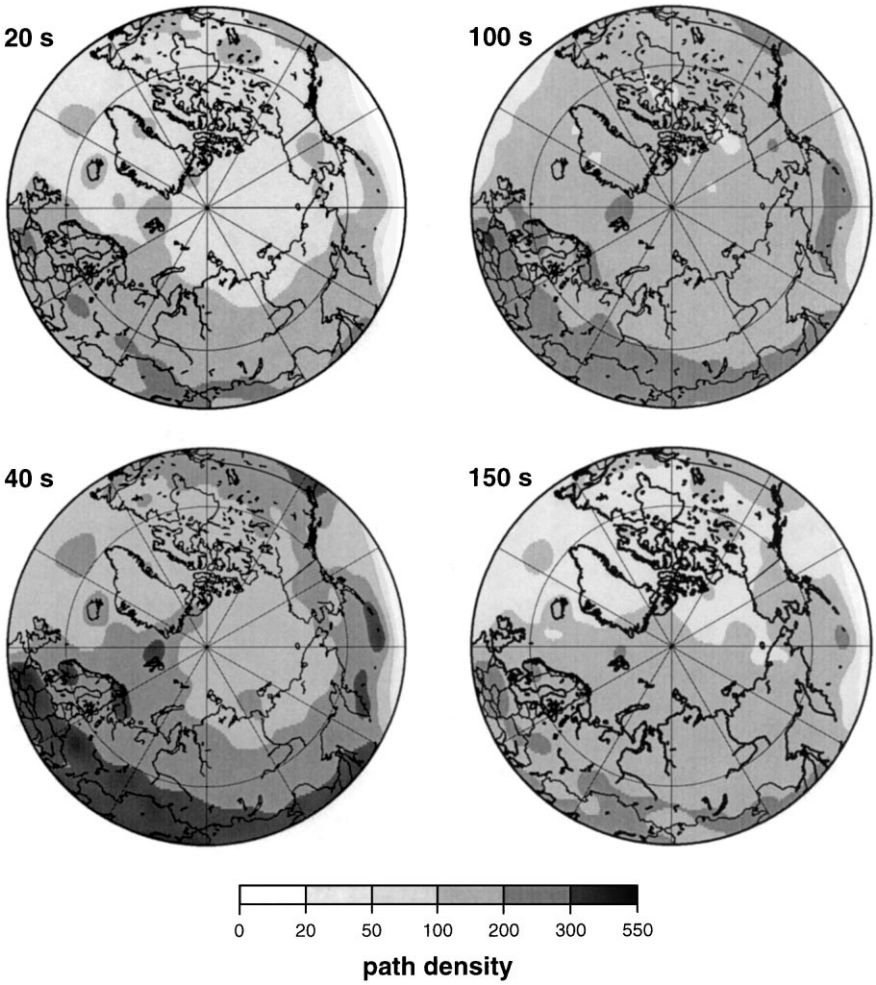

Fig. 3. Path density for Rayleigh waves at the four indicated periods. Path density is defined as the number of rays intersecting a 2° square cell (~50,000 km^2).

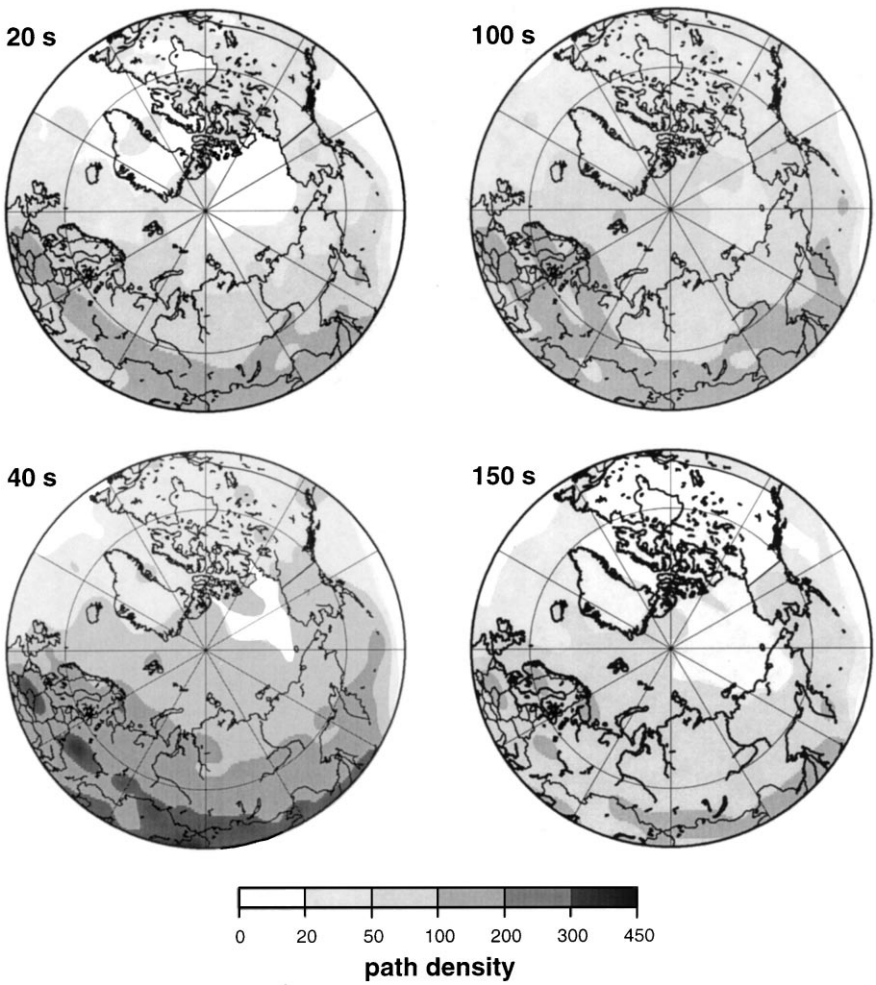

Fig. 4. Path density for Love waves. See Fig. 3 for a definition.

Path densities at different periods for both Rayleigh and Love waves are shown in Figs. 3 and 4. For Rayleigh waves, path densities are high across most of the region north of the 60°N latitude, but are higher in the eastern hemisphere due to the large number of measurements we obtained as part of an on-going study of Eurasia (e.g. Ritzwoller and Levshin, 1998). Path densities for Love waves are generally lower than for Rayleigh waves, particularly in North America, again due to the priorities of previous studies.

The procedure for estimating P_n and S_n maps follows that described by Ritzwoller et al. (2000). P_n and S_n travel times are taken from a groomed version of the ISC and NEIC data bases described, in part, by Engdahl et al. (1998). ISC travel times are for events that occurred from 1964 to 1997 and NEIC data are from 1998 to 1999. The locations of the events are replaced with local ground truth locations whenever possible (e.g. Sultanov et al., 1999). We define the phases P_n and S_n as arriving between epicentral distances of 3 and 15°. Truncation of the data set to include rays only for shorter maximum epicentral distances (e.g. Hearn and Ni, 1994), severely restricts path coverage in the Arctic.

Data are selected for analysis if the residual relative to the prediction from the spherical model ak135 (Kennett et al., 1995) is less than 7.5 s for P and 15 s for S, if the event depth is within the crust or <50 km

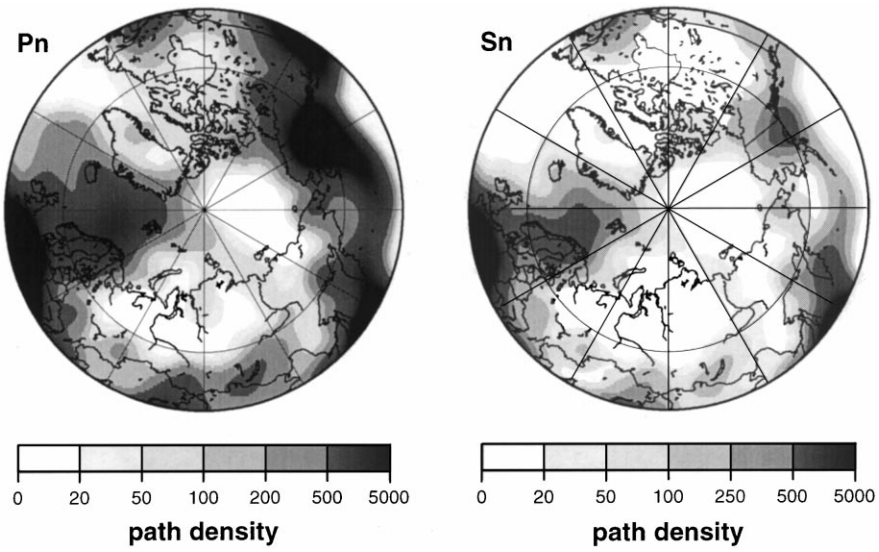

Fig. 5. Path density for P_n and S_n. See Fig. 3 for a definition.

deep, if the azimuthal gap to all reporting stations for the event is $<180^\circ$, and if the nominal error ellipse is $<1000\,\mathrm{km}^2$ in area. In order to reject late arriving phases (e.g. *PmP*, P_b, *SmS*, S_b) misidentified as P_n or S_n we apply a stricter misfit threshold between epicentral distances from 3 to 7°. Altogether, about 1,132,500 P_n travel times and 310,800 S_n travel times are left for tomographic inversion across the Arctic (latitudes higher than 50°N). Path densities are shown in Fig. 5.

3. Tomographic method

The group velocity maps and the P_n and S_n maps are defined over a two-dimensional surface (latitude θ, longitude ϕ). Thus, they may be estimated with the same tomographic method. We use the method of Barmin et al. (2000). In this method, the model is constructed on an equally spaced grid such that the following figure-of-merit is minimized:

$$(\boldsymbol{Gm}-\boldsymbol{d})^{\mathrm{T}}C^{-1}(\boldsymbol{Gm}-\boldsymbol{d})+\sum_{k=0}^{n}\alpha_k^2||F_k(\boldsymbol{m})||^2 +\sum_{k=0}^{n}\beta_k^2||H_k(\boldsymbol{m})||^2, \quad (1)$$

which is a linear combination of data misfit, model roughness, and the amplitude of the perturbation to a reference model. The vector $\boldsymbol{m}$ represents the estimated model over the region of interest, i.e. values of velocity perturbations relative to the reference model at grid points. $\boldsymbol{G}$ is the forward operator that computes travel time from the estimated model, $\boldsymbol{d}$ the data vector which components are observed travel time residuals relative to the reference model, $\boldsymbol{C}$ the data covariance matrix or matrix of data weights, F a Gaussian smoothing operator, and H an operator that penalizes the norm of the model in regions of poor path coverage for the isotropic component of the model or poor azimuthal coverage for the anisotropic model coefficients. The model $\boldsymbol{m}$ is azimuthally anisotropic such that m_0 is an isotropic perturbation to the reference model and $m_1,\ldots,m_4$ represent azimuthally anisotropic perturbations (Smith and Dahlen, 1973; Trampert and Woodhouse, 1996)

$$m(\boldsymbol{r},\Psi)=m_0(\boldsymbol{r})+m_1(\boldsymbol{r})\cos 2\Psi+m_2(\boldsymbol{r})\sin 2\Psi +m_3(\boldsymbol{r})\cos 4\Psi+m_4(\boldsymbol{r})\sin 4\Psi, \quad (2)$$

where $\boldsymbol{r}=(\theta,\phi)$, and Ψ is the azimuth of the wave path at point $\boldsymbol{r}$. The spatial smoothing operator is defined over the 2-D model as follows:

$$F_k(\boldsymbol{m}) = m_k(\boldsymbol{r}) - \int_S S_k(\boldsymbol{r}, \boldsymbol{r}') m_k(\boldsymbol{r}')\, \mathrm{d}\boldsymbol{r}', \tag{3}$$

where S_k is a smoothing kernel.

$$S_k(\boldsymbol{r}, \boldsymbol{r}') = K_{0k} \exp\left(-\frac{|\boldsymbol{r} - \boldsymbol{r}'|^2}{2\sigma_k^2}\right) \tag{4}$$

$$\int_S S_k(\boldsymbol{r}, \boldsymbol{r}')\, \mathrm{d}\boldsymbol{r}' = 1, \tag{5}$$

and σ_k is the spatial smoothing width or correlation length.

The final term in the penalty function penalizes the weighted norm of the model

$$H_k(\boldsymbol{m}) = \mathcal{H}(\rho(\boldsymbol{r}), \chi(\boldsymbol{r})) m_k, \tag{6}$$

where $\mathcal{H}$ is a weighting function that depends on local path density ρ for isotropic structure and a measure of local azimuthal distribution χ for azimuthal anisotropy. Thus, for $k = 0$, $\mathcal{H} = \mathcal{H}(\rho)$ and for $k = 1, \ldots, 4$, $\mathcal{H} = \mathcal{H}(\chi)$. Path density is defined as the number of paths intersecting a circle of fixed radius with center at the point $\boldsymbol{r}$. For isotropic structure, we choose $\mathcal{H}$ to approach 0 where path density is suitably high and unity in areas of poor path coverage. The function $\mathcal{H}(\rho)$ can be chosen in various ways. We use $\mathcal{H} = \exp(-\lambda\rho)$, where λ is a user defined constant. To damp azimuthal anisotropy in regions with poor azimuthal coverage, we define $\chi(\theta, \phi)$ to measure the azimuthal distribution of ray paths at point (θ, ϕ). To find χ, we construct a histogram of azimuthal distribution of ray paths in the vicinity of (θ, ϕ) for a fixed number n of azimuthal bins in the interval between 0 and 180°, and evaluate the function

$$\chi = \frac{\sum_{i=1}^{n} f_i}{n \max_i f_i}, \tag{7}$$

where f_i is the density of azimuths in the ith bin. Values of χ are in the range $1/n \le \chi \le 1$. $\chi \approx 1$ characterizes an almost uniform distribution of azimuths, and $\chi \approx 1/n$ is an indicator of the predominance of a single azimuthal direction (large azimuthal gap). We assume that the anisotropic coefficients cannot be determined reliably in regions where χ is less than ~0.3.

The minimization of the expression in Eq. (1) explicitly ensures that the estimated model approximates a smoothed version of the model.

The inversion for P_n and S_n is described in detail by Ritzwoller et al. (2000). The observed travel P_n or S_n time, t_{obs}, is modeled as follows:

$$t_{\mathrm{obs}} = t_{\mathrm{m}} + t_{\mathrm{crust\_sta}} + t_{\mathrm{crust\_evt}} + \delta t_{\mathrm{sta}} + \delta t_{\mathrm{evt}} + \delta t(\Delta) + \delta t_{\mathrm{m}}, \tag{8}$$

where t_{m} is the predicted travel time for rays through the mantle part of the input reference model, the contributions to the travel time due to the crustal part of the reference model on the event and station sides are $t_{\mathrm{crust\_sta}}$ and $t_{\mathrm{crust\_evt}}$, the station and event statics are δt_{sta} and δt_{evt}, $\delta t(\Delta)$ is the distance correction, δt_{m} is the travel time correction for the mantle part of the path, and Δ is epicentral distance. Thus, t_{m}, $t_{\mathrm{crust\_sta}}$, and $t_{\mathrm{crust\_evt}}$ are predicted by the reference model and δt_{sta}, δt_{evt}, $\delta t(\Delta)$, and δt_{m} are estimated. If v_{m} is the velocity along path p in the reference model and δv_{m} is the model perturbation along the same path, then

$$t_{\mathrm{m}} = \int_p \frac{\mathrm{d}s}{v_{\mathrm{m}}} \tag{9}$$

$$\delta t_{\mathrm{m}} = -\int_p \frac{\delta v_{\mathrm{m}}}{v_{\mathrm{m}}^2}\, \mathrm{d}s. \tag{10}$$

We assume that the ray through the perturbed model, $v_{\mathrm{m}} + \delta v_{\mathrm{m}}$, takes the same path as the ray through the reference model. In practice, we estimate the 2-D quantity δv_{m} from which we compute δt_{m} for each ray p.

We used CRUST5.1 (Mooney et al., 1998) as the reference model in the crust and for mantle P and S. At each geographical point, CRUST5.1 only has one value of P and one value of S for the mantle, intended to characterize the velocity immediately below Moho. For this reason, we assume that the mantle leg of each path p is essentially horizontal, following directly below Moho. Although this is a common approximation in P_n and S_n tomography, it introduces an error relative to real rays that depends on the depth of penetration of the ray, which itself depends on the vertical gradient of velocity in the mantle. To compensate for this error, we introduce into Eq. (8) a term that is a smooth function of distance, which we call the distance correction, $\delta t(\Delta)$. The correction $\delta t(\Delta)$, therefore, attempts to reduce the mantle velocities distributed in 3-D to a single 2-D datum surface which, by design, lies directly below Moho. The distance correction is

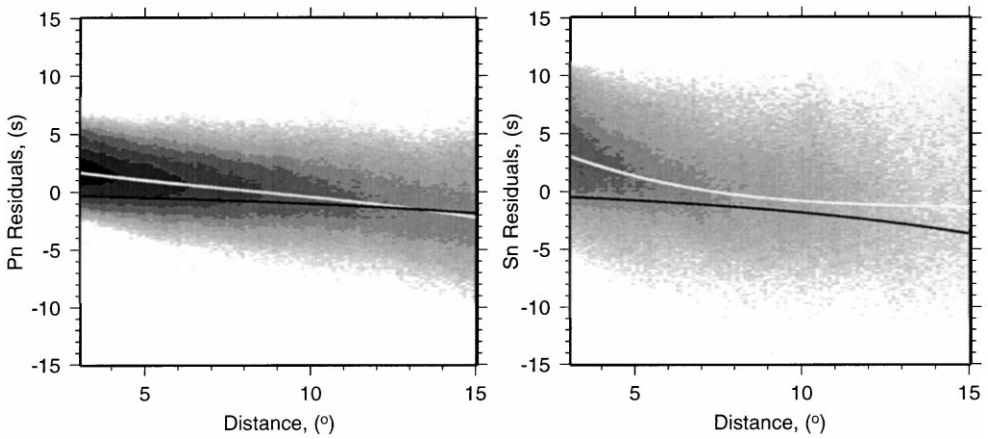

Fig. 6. Shaded plots of the density of P_n and S_n travel time residuals (observed minus predicted from CRUST5.1) versus epicentral distance with respect to CRUST5.1. White lines are the estimated trends of P_n and S_n travel times versus epicentral distance that are used for the distance corrections, $\delta t(\Delta)$. Black lines are similar trends predicted for the model ak135.

shown in Fig. 6 along with the density of residuals for P_n and S_n travel times relative to the reference model.

The application of the distance correction allows us to fit data over a broader distance range than would be possible without the correction. We find that with this correction, the tomographic maps agree well with those produced with short path data alone (epicentral distances $<10^\circ$) in those regions where tomographic maps can be constructed reliably using only the short path data.

We follow Hearn and collaborators (e.g. Hearn and Clayton, 1986; Hearn et al., 1991; Hearn and Ni, 1994; and elsewhere) and estimate event and station corrections or statics. The station and event statics are designed to compensate for errors in the reference crustal model, errors in the prediction of the location of the mantle piercing points, and errors in event locations and origin times. A static correction is estimated for a station if there are phase picks from at least seven events made at that station and an event correction is estimated for all events for which there are at least 20 reporting stations. The asymmetry in this condition is due to the fact that there are more physical phenomena modeled with the event static than with the station static (e.g. mislocation, origin time error). The station and event statics are undamped at present.

There are, therefore, many parameters that need to be set to estimate a 2-D map, including grid spacing, $\alpha_0, \ldots, \alpha_4$, $\sigma_0, \ldots, \sigma_4$, and $\beta_0, \ldots, \beta_4$. In practice, the model norm damping constants are all set to the same value $\beta_k = \beta = 1$, and the anisotropic damping constants and correlation lengths are also equal $\sigma_{\text{anis}} = \sigma_1 = \sigma_2$ and $\alpha_{\text{anis}} = \alpha_1 = \alpha_2$. We estimate only the 2Ψ component of azimuthal anisotropy here, so α_3, α_4, σ_3, and σ_4 are all effectively infinite. The parameters used here are shown in Table 1 where U is group velocity, and a dash indicates that the structure was not estimated for the specified map, and all units are kilometer.

4. Isotropic group velocity, P_n, and S_n tomography

The estimated maps are perturbations to the predictions from a reference model. For group velocities, the reference model is a smoothed version of a hybrid model composed of CRUST5.1 in the crust and S16B30 in the mantle. For P_n and S_n, the reference model is CRUST5.1. As Barmin et al. (2000) show, estimates of spatial resolution and amplitude bias are obtained as by-products of the inversion. We do not discuss these estimates here, but merely state some of the results of the resolution analysis.

As discussed by Ritzwoller and Levshin (1998), the principal source of error in the estimated group velocity maps is expected to be caused by errors in the

Table 1
Table of inversion parameters[a]

Wave-type	σ_0	σ_{anis}	α_0	α_{anis}	Isotropic grid-spacing	Anisotropic grid-spacing
U	200	600	1000 if <100 s, 1300 if ≥ 100 s	1500, 3000, 5000	200	250
P_n	100	–	600	–	100	–
S_n	100	–	600	–	100	–

[a] All units are in km.

theory that underlies the tomography rather than errors in the data themselves. Measurement errors are fairly well-reduced by the data cleaning procedure discussed in Section 2. Ritzwoller and Levshin (1998) discussed four theoretical errors that may potentially affect the results of a tomographic study. Our recent improvements in the tomographic algorithm have effectively eliminated two of these problems: geometrical distortions due to earth flattening approximations and the bias of isotropic structures caused by azimuthal anisotropy. The first has been eliminated by formulating the inversion in spherical coordinates from the outset. The second has been greatly attenuated by simultaneously estimating azimuthal anisotropy with isotropic velocities. The remaining two problems are the mislocation of seismic events and deviation of surface waves from great circle paths. The effects of event mislocation are shown by Ritzwoller and Levshin (1998) to only be important at the periphery of a studied region because data from paths crossing the region containing mislocated events constrain the errors caused by the mislocations. Thus, the major remaining theoretical error that may be of sufficient magnitude to bias the estimated maps is the deviation of surface waves from great circle paths. An evaluation of the bias caused by this effect and attempts to reduce it are the subject of current research. The effect is expected to be most significant at short and intermediate periods (<50 s) where lateral heterogeneities in the phase velocities are strongest. It will manifest itself as a smearing of the maps in regions of strong heterogeneity that will result in a reduced effective resolution precisely in the most interesting regions.

We estimated group velocity maps for Rayleigh waves at periods from 15 to 200 s and for Love waves from 20 to 125 s. A selection of these maps is shown in Fig. 7 (Rayleigh waves) and Fig. 8 (Love waves). The spatial resolution changes geographically and with period, but in general is reasonably good; 300–500 km between 20 and 150 s for Rayleigh waves, but worse everywhere for Love waves particularly at very short and very long periods.

The estimated P_n and S_n maps are shown in Fig. 9. As discussed above, our tomographic method penalizes the amplitude of the maps in regions of poor data coverage. Because the estimated maps are perturbations to a reference state, the maps will revert to the reference model where data coverage is poor, i.e. $<$15–20 paths for each $2 \times 2^\circ$ cell. Except for the shortest period Love waves, the vast majority of the group velocity maps shown in Figs. 7 and 8 display sufficient coverage to guarantee that they will be independent of the reference model. This is not true for the P_n and S_n maps because, by definition, these phases only exist to an epicentral distance of 15°. There are large regions of the Arctic in which either earthquakes do not regularly occur or there have been few historical seismic stations that reported phase picks to the ISC. As a result, we identify areas of poor data coverage in Fig. 9 as gray-shaded regions. The S_n map, in particular, is very patchy, but we show it for comparison with P_n map in regions where there is sufficient data coverage. The spatial resolution of the P_n map is about 250–350 km in northern Europe, the North Atlantic, and along the Arctic Ocean coasts in the Bering Sea, off Alaska and western Canada. It is between 400 and 450 km along the Arctic mid-oceanic ridge. Other regions, such as north-western Siberia or the Amerasia Basin, possess path densities below about 20 paths per $2 \times 2^\circ$ cell and are very poorly resolved.

Misfit statistics for the isotropic maps are presented in Table 2. RMS misfit is presented relative to the two reference models. Misfit for P_n and S_n is computed after noisy measurements have been rejected using a 2σ criterion.

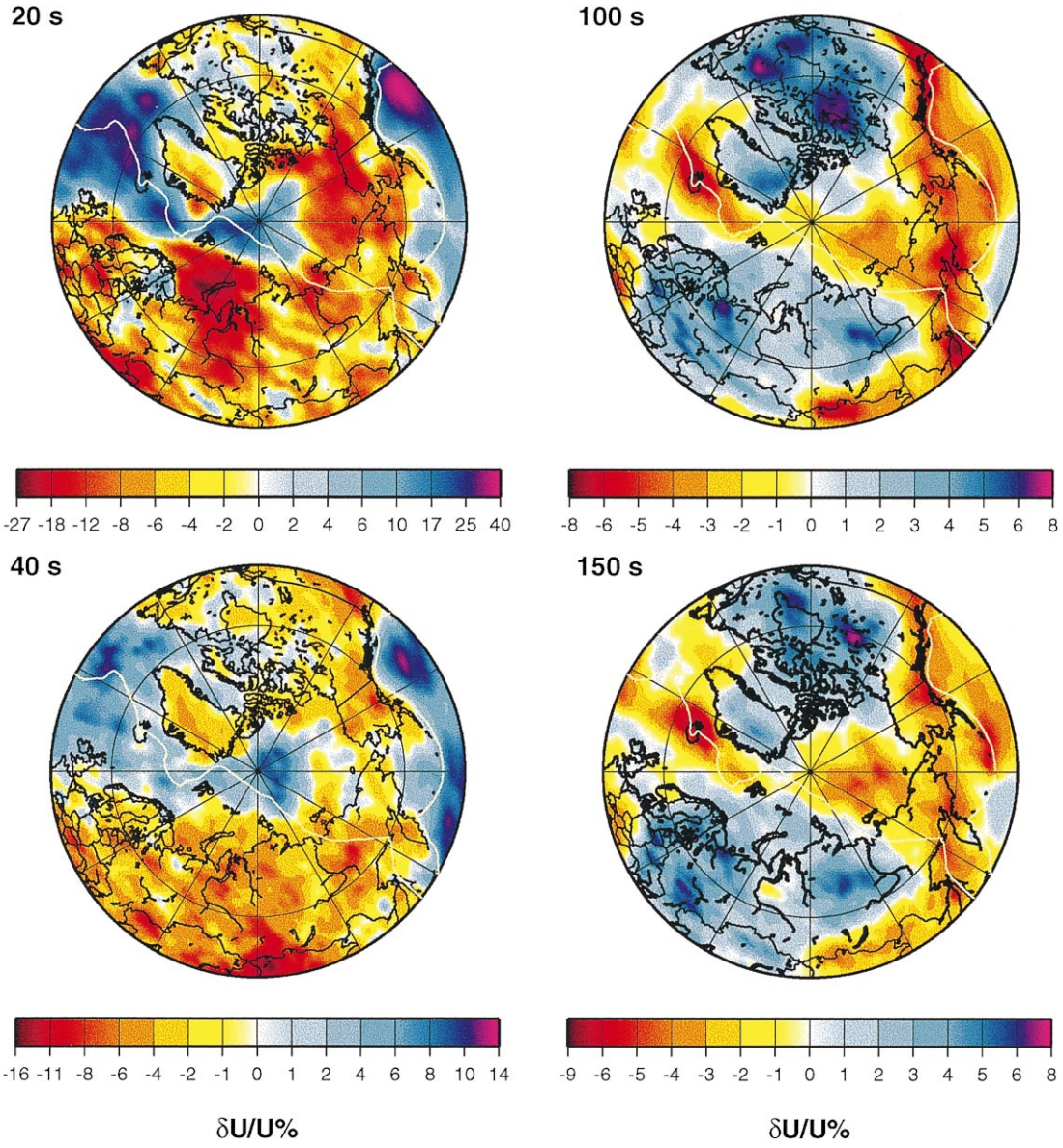

Fig. 7. Estimated Rayleigh wave group velocity maps at the indicated periods. $\delta U/U$ is the relative deviation of group velocity from the average value U across the map (in %). White lines are plate boundaries. Reference velocities are as follows: 20 s–3.103 km/s; 40 s–3.739 km/s; 100 s–3.848 km/s; 150 s–3.754 km/s.

5. Azimuthal anisotropy

Simultaneous with the isotropic maps we have estimated 2Ψ anisotropic maps for group velocity following the procedure described by Barmin et al. (2000). This procedure allows us to apply different relative damping parameters, α_0 and α_{anis}, to the isotropic and anisotropic terms of the estimated model. The larger the values of the damping parameters, the smoother will be the resulting maps.

As shown in Fig. 10, strong damping of anisotropy produces a very long wavelength pattern of azimuthal

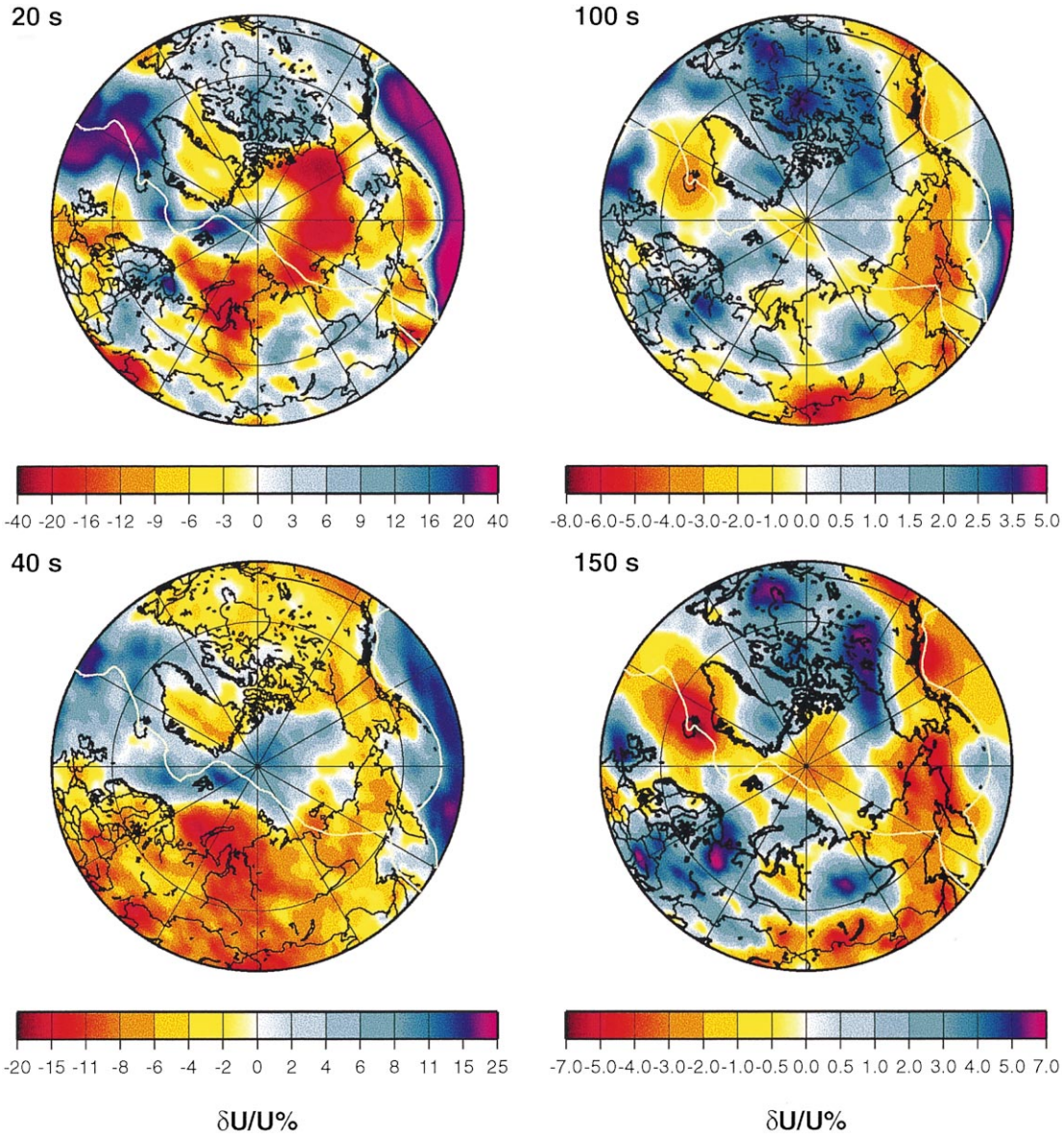

Fig. 8. Estimated Love wave group velocity maps at the indicated periods. Reference velocities are as follows: 20 s–3.307 km/s; 40 s–3.999 km/s; 100 s–4.391 km/s; 150 s–4.432 km/s.

anisotropy in group velocity similar to the pattern obtained in the global scale phase velocity study of Trampert and Woodhouse (1996). In this figure, our 50 and 100 s group velocity maps are compared with the global scale 40 and 80 s phase velocity maps. The differences in the period between the group and phase velocity maps is designed to compensate partially for the fact that phase velocities sample deeper than group velocities at a particular period.

To quantify the correlation between two maps of azimuthal anisotropy, we use the coherence function defined by Griot et al. (1998) which takes into account differences in the directions of the fast axes ($\psi_1(\theta,\phi)$, $\psi_2(\theta,\phi)$) and the amplitudes ($A_1(\theta,\phi)$, $A_2(\theta,\phi)$; $A =$

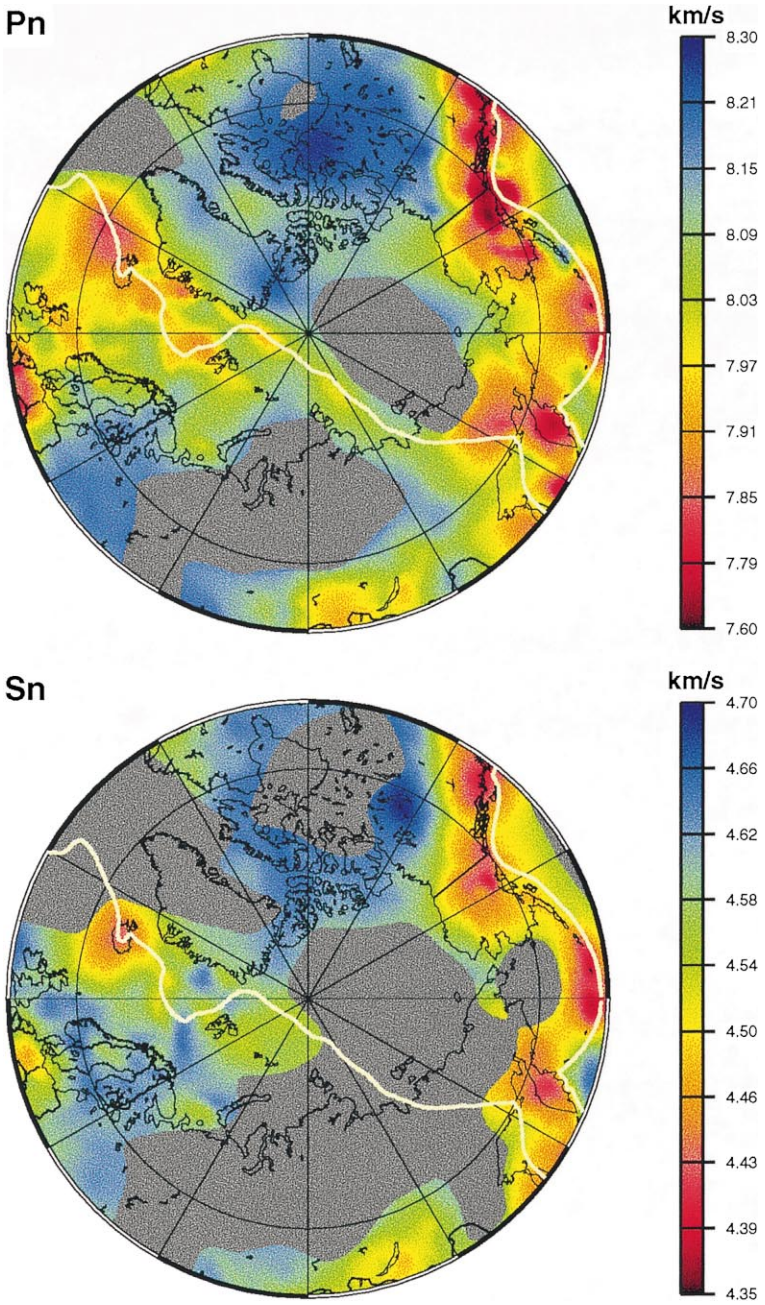

Fig. 9. P_n and S_n velocities across the Arctic region. Units are km/s. Gray areas have path densities <20 paths per a 2° square cell.

Table 2
Misfits between observed and predicted values of group velocities/travel times before and after inversion

Wave-type	Reference model $\overline{\delta U}$ (km/s)[a]	After inversion $\overline{\delta U}$ (km/s)	Variance reduction (%)
Rayleigh 20 s group	0.128	0.089	51
Rayleigh 40 s group	0.133	0.067	75
Rayleigh 100 s group	0.076	0.050	58
Rayleigh 150 s group	0.067	0.058	25
Love 20 s group	0.209	0.154	46
Love 40 s group	0.109	0.077	50
Love 100 s group	0.086	0.054	61
Love 150 s group	0.122	0.086	25
	$\overline{\delta t}$ (s)[b]	$\overline{\delta t}$ (s)	
P_n	2.14	1.35	60
S_n	3.70	2.60	50

[a] CRUST5.1 + S16B30.
[b] CRUST5.1.

$(U_1^2 + U_2^2)^{1/2}$) of the two maps. The coherence K as a function of rotation angle ψ, varying between -90 and 90°, is defined as follows:

$$K(\psi) = \frac{\sum_\theta \sum_\phi A_1(\theta,\phi) A_2(\theta,\phi) \sin\theta \exp(-(\psi_1(\theta,\phi) - \psi_2(\theta,\phi) + \psi)^2 / 2D_{\text{cor}}^2)}{\left(\sum_\theta \sum_\phi \sin\theta\, A_1^2(\theta,\phi)\right)^{1/2} \left(\sum_\theta \sum_\phi \sin\theta\, A_2^2(\theta,\phi)\right)^{1/2}}. \quad (11)$$

Here, D_{cor} is the uncertainty in the anisotropic direction, and was set to equal 10°. The coherence between the group velocity and the phase velocity maps shown in Fig. 10 is displayed as the solid lines in Fig. 11a and b. If the correlation between the group and phase velocity maps were perfect, the coherence functions would peak with unit amplitude at a differential angle of 0° and would display no side-lobes. For the comparison between the 100 s group velocity and the 80 s phase velocity (Fig. 10b), the coherence function peaks at about -4° with an amplitude of 0.35 and a side-lobe centered at about $\pm 90^\circ$. This represents substantial similarity between the two maps.

Although the long wavelength part of the estimated group velocity maps is in substantial agreement with the global study of Trampert and Woodhouse, the information content in these maps is low. We would like to reduce the scale of the estimated variations in azimuthal anisotropy in a stable, continuous way in the attempt to reveal more information about the variations in the fabric and mineral orientation of the uppermost mantle. To do so, the damping of azimuthal anisotropy must be reduced which will make the estimates more sensitive to noise, both signal generated and other.

The anisotropic damping parameter for the group velocity maps shown in Fig. 10 is $\alpha_{\text{anis}} = 5000$. When we reduce α_{anis} from 5000 to 3000 and then to 1500 the correlation with the global model degrades dramatically, as the dashed and dotted lines in Fig. 11a and b demonstrate. The coherence between our estimated maps also changes strongly as the damping parameters are reduced as shown in Fig. 11c and d. Thus, both the pattern and amplitude of anisotropy are affected by the choice of the strength of damping. However, isotropic maps do not change significantly with changes of α_{anis}. As a rule, they became slightly more smooth as α_{anis} decreases. Overall RMS misfit statistics for the isotropic model, the isotropic model with smooth azimuthal anisotropy, and the isotropic model with smaller scale azimuthal anisotropy are presented in Table 3. Typically, RMS misfit reductions are much easier to achieve by reducing the damping of the isotropic model than by introducing azimuthal anisotropy.

The resulting Rayleigh wave group velocity maps at 50 and 100 s period for moderate damping ($\alpha_{\text{anis}} =$

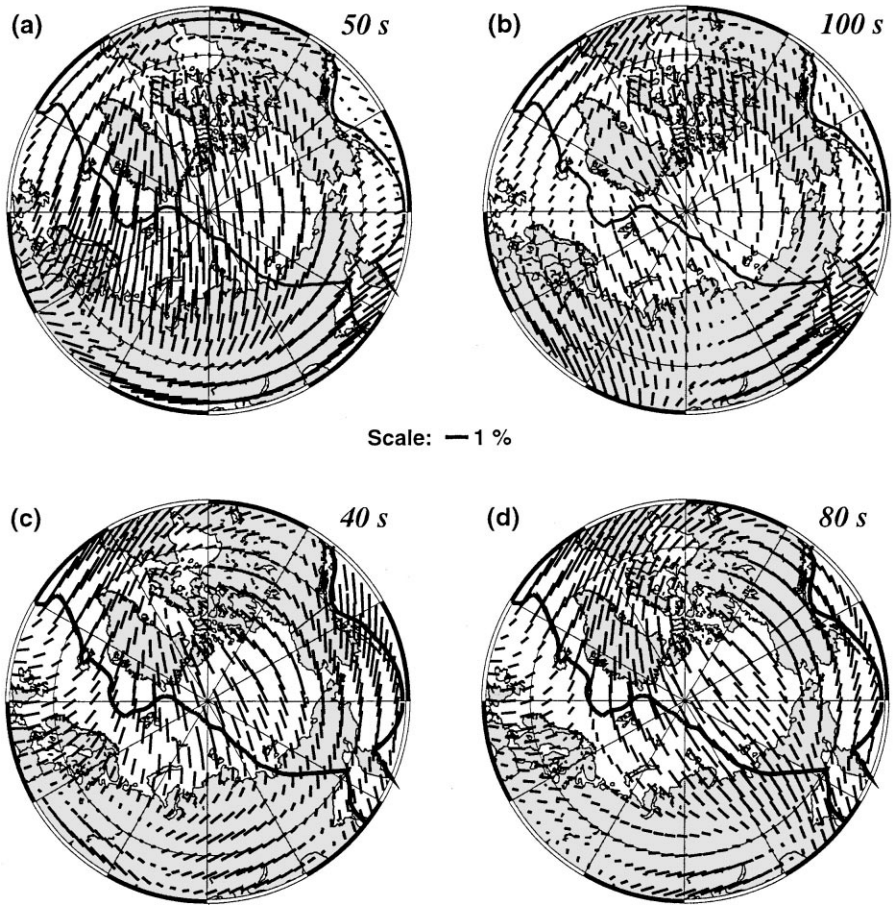

Fig. 10. The 2Ψ component of azimuthal anisotropy of Rayleigh wave group velocity at the indicated periods. (a, b) Strongly damped group velocity ($\alpha_{\text{anis}} = 5000$). (c, d) Phase velocity from Trampert and Woodhouse (1996). The bars indicate the 2Ψ fast directions. The size of the bars is proportional to the ratio of the anisotropic and the isotropic components.

1500) are shown in Fig. 12. In these maps, in contrast with those in Fig. 10, the largest anomalies are associated with the Baltic, Siberian and Canadian shields and the fast directions in the Arctic Ocean are nearly perpendicular to those in the highly damped maps in Fig. 10. In addition, the fast directions are predominantly perpendicular to plate boundaries along the Atlantic mid-oceanic ridge (MOR) and in the Bering Sea along the Aleutian Arc, but are almost parallel to the Arctic MOR. This may be due to mineral orientation caused by relatively fast plate motions in the Atlantic and north-western Pacific and much slower speeds in the Arctic Ocean. Finally, as demonstrated in Fig. 13, the patterns of anisotropy in the 50 and 100 s Rayleigh wave maps are exceptionally well-correlated, which may indicate the continuity of the pattern of anisotropy at least through 100–150 km of the uppermost mantle for a significant part of the studied area (North America, Greenland, the Baltic shield, some parts of the northern Eurasia).

Although the high correlation between the long wavelength component of our regional scale group velocity maps with the global scale phase velocity maps of Trampert and Woodhouse is encouraging, the strong dependence of the estimated maps on arbitrarily chosen damping parameters should give us pause in attempting to interpret the maps quantitatively.

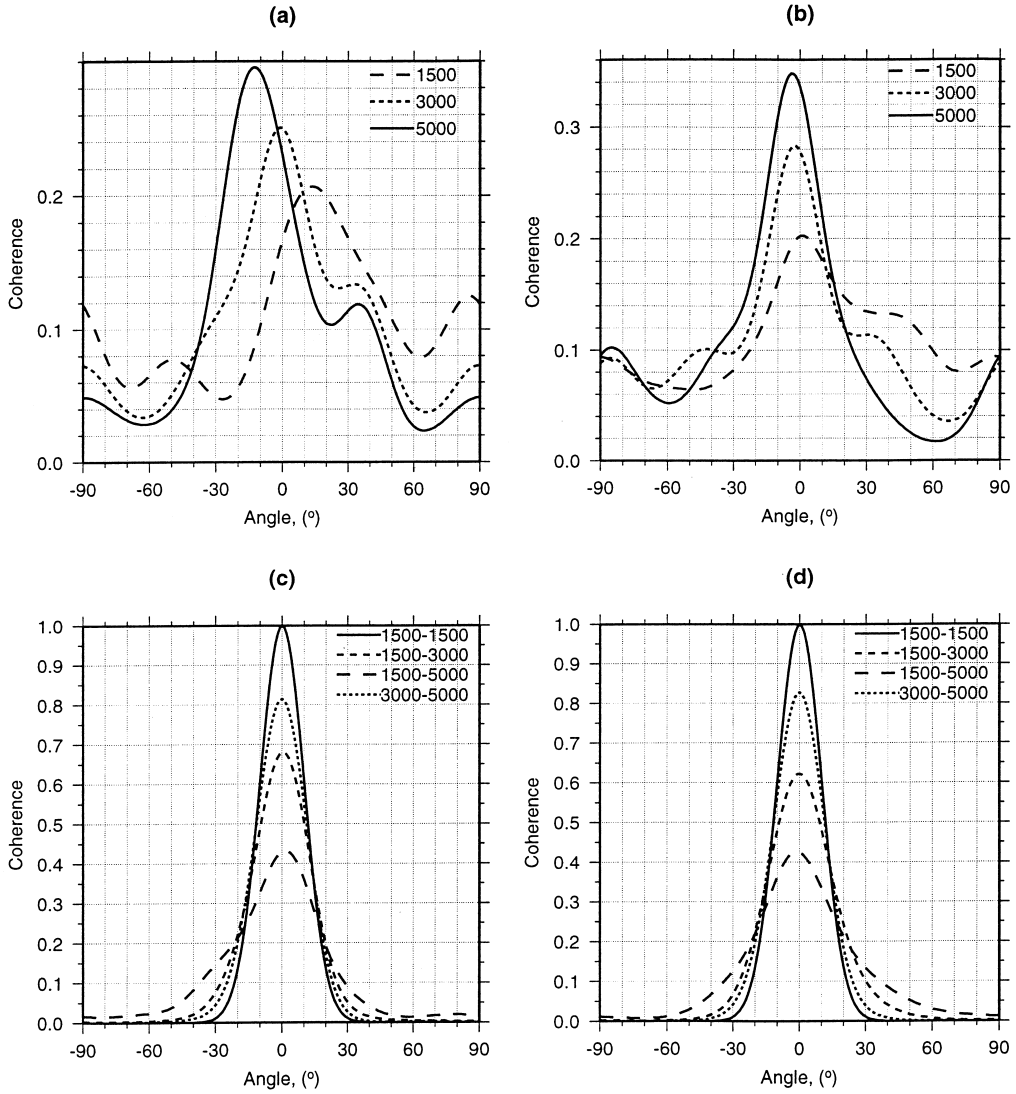

Fig. 11. The influence of damping on the coherence between Rayleigh wave 2Ψ azimuthal anisotropy maps. (a) Coherence between group velocity anisotropy maps at 50 s period and the global phase velocity anisotropy map at 40 s. Several dampings of the group velocity maps are shown. (b) Similar to (a) but here is the coherence between group velocity anisotropy maps at 100 s period at a variety of dampings and the global phase velocity anisotropy map at 80 s. (c) Coherence between our estimated Rayleigh wave group velocity anisotropy maps at 50 s period obtained using different damping parameters. Contrast the result for self-coherence (solid line). (d) Same as (c), but for the 100 s Rayleigh wave. Numbers in the upper right corner of each graph indicate the magnitude of the damping parameter α_{anis}.

Table 3
Misfit between observed and predicted values of group velocities of Rayleigh waves for isotropic and anisotropic models (km/s)

Period (s)	Isotropic model	Isotropic + smoothed anisotropic model	Isotropic + fine anisotropic model
50	0.062	0.061	0.057
100	0.050	0.049	0.046

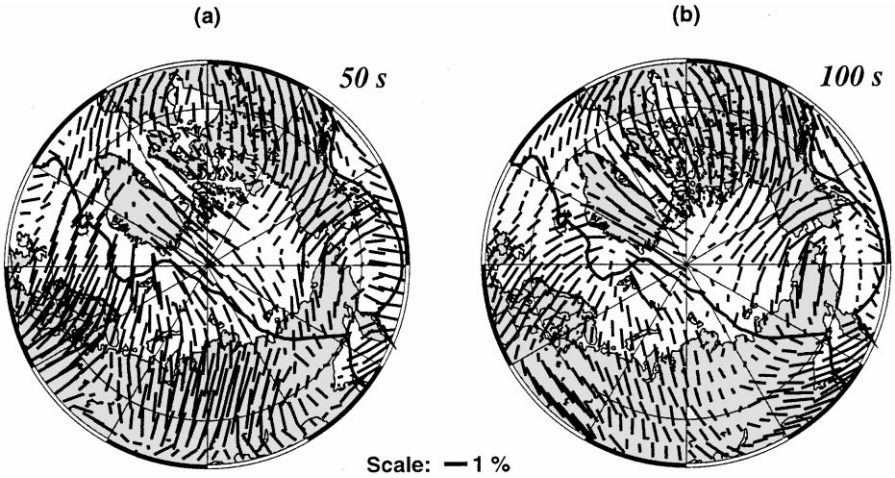

Fig. 12. Estimated 2Ψ azimuthal anisotropy of Rayleigh wave group velocity at the indicated periods for moderate damping of anisotropy ($\alpha_{\text{anis}} = 1500$). (a) 50 s period and (b) 100 s period.

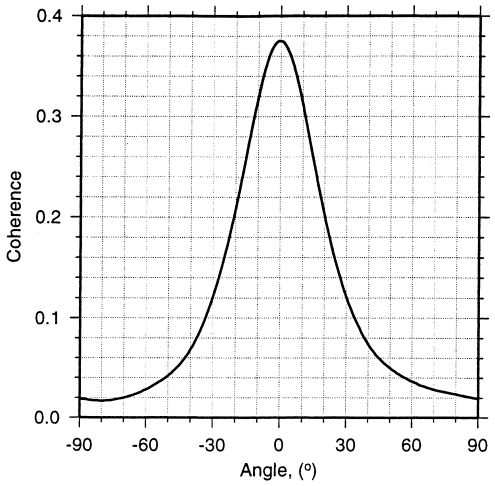

Fig. 13. Coherence between the two maps shown in Fig. 12.

6. Discussion

Isotropic group velocity maps provide strong constraints on the shear velocity of the crust and upper mantle and on crustal thickness across the Arctic. Because group velocity sensitivity kernels are more complicated than phase velocity kernels (e.g. Rodi et al., 1975), interpreting them directly in terms of causative structures is not entirely straight-forward. However, our experience with the inverse problem in various regions around the world (e.g. Villaseñor et al., 2001) indicates that the maps at certain periods do identify some of the key elements of the model. For example, low velocity anomalies on the 20 s maps are typically associated with sedimentary basins. Anomalies on the 40 s maps are inversely related to crustal thicknesses in continental areas so that low velocities typically imply thick continental crust and high velocities imply thin crust. The 40 s map predominantly samples the upper mantle under oceanic areas. At periods of 100 s and above, the maps are preferentially sensitive to the uppermost mantle beneath both continents and oceans. With these observations in mind, it is worth noting the major features on the isotropic group velocity maps and what they may mean.

Nearly all of the major sedimentary basins seen in Fig. 14 (Laske and Masters, 1997) are associated with low velocities on the 20 s Rayleigh and Love wave group velocity maps. These include sedimentary basins in the Chukchi and Beaufort Seas, the Lincoln Sea north of Greenland, Baffin Bay, the Greenland Sea, the Barents Sea, the Kara Sea, and the E. Siberian Sea. The observation of distinct low velocity anomalies associated with relatively small

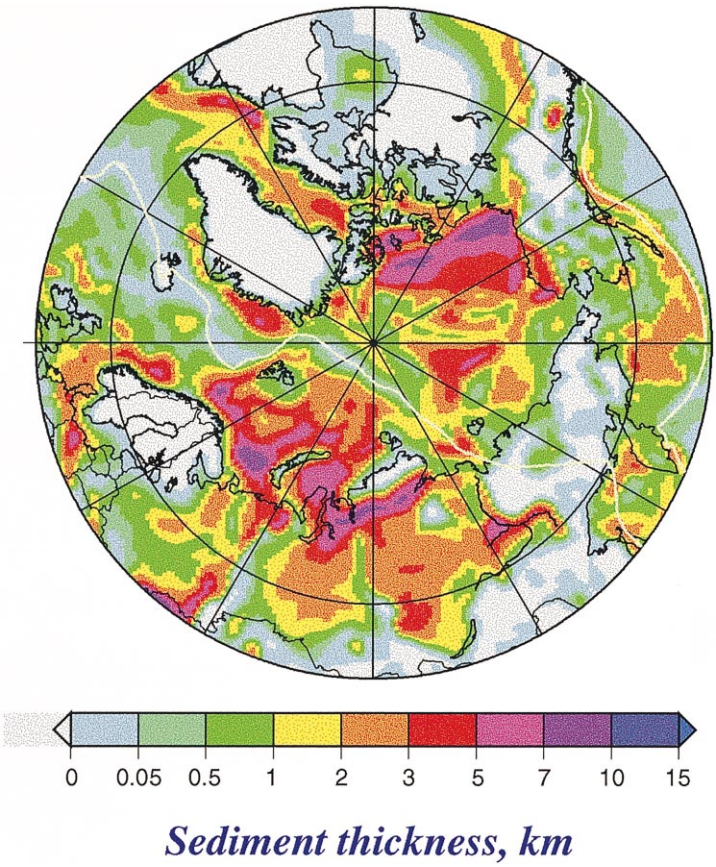

Fig. 14. Thickness of sediments across the Arctic (Laske and Masters, 1997).

basins in the Lincoln and Greenland Seas north and east of Greenland, respectively, clearly characterizes the spatial resolution of the group velocity maps. Our studies of Central Asia (Ritzwoller and Levshin, 1998; Ritzwoller et al., 1998) demonstrated that periods shorter than 20 s will produce even better images of sedimentary basins. Unfortunately, our data set at shorter periods needs to be developed further before we are able to obtain these maps. In continental regions, in particular, age, chemical composition, lithology, and the tectonic history of the sediments also influence group velocities. Some sedimentary basins, e.g. the Enisei–Khatanga trough in northern Siberia, do not appear as low velocity anomalies on the short period group velocity maps due to partial metamorphism of the sediments and interpenetration of the sediments with trap basalts.

The Amerasia and Eurasia Basins are imaged at 20 and 40 s period in Figs. 7 and 8. The high velocity anomaly coincident with the Eurasia Basin extends nearly to the continental shelf on the 40 s map all around the Arctic Ocean. The shape of the Amerasia Basin on the 40 s map also appears to be fairly accurately resolved.

We clearly observe continental low velocity anomalies on the 40 s Rayleigh wave map which typically signify regions of thickened crust. Low velocity anomalies are associated with the Verkhoy anski range, the Chersky range, Kamchatka, the Koryakia and Okhotsk–Chuckotsk volcanic belts in north-eastern Siberia, as well as the Brooks range, the Alaska range, and Yukon plateau in northern America.

Mid-ocean ridges appear in Rayleigh wave group velocity maps around the world at periods of 40 s

and above. The Arctic MOR, however, does not manifest itself on the 40 s Rayleigh wave map in Fig. 7. Oceanic low velocity anomalies of mantle origin do not appear in the Arctic until nearer to 100 s period. This is typical of slower spreading ridges. There are, however, two significant Artic low velocity anomalies at long periods. The first and more prominent is associated with the Iceland hotspot and the northward continuation of this anomaly adjacent to the Mohns Ridge toward the Fram Strait between Greenland and Svalbard. The thermal halo of this hot spot in the mantle, manifested as a low velocity anomaly in most of the dispersion maps, is considerably broader than the surface expression of the hot spot. The second anomaly runs from the Laptev Sea to the Mendeleev Ridge. Interestingly, this anomaly is not obviously coincident with the seismically active Arctic MOR. At 150 s period, the low velocities are more nearly coincident with the aseismic Mendeleev Ridge.

There are two very striking features on the long period maps under continents at high latitudes. The first is the expression of the continental shields. The Russian Platform, Siberian Shield, Canadian Shield, and Greenland Shield are imaged clearly on the 100 and 150 s Rayleigh and Love wave maps in Figs. 7 and 8. The two large Asian shields are separated by a relative low velocity anomaly adjacent to the Urals that becomes more pronounced at longer periods. The second striking feature is the low velocity anomaly that follows the Pacific Rim of Asia from Taiwan to Kamchatka. Fig. 7 shows that this feature probably extends to the Pacific Rim of North America along the Alaskan and Canadian coasts.

Because the long-period (e.g. 100 s period) Rayleigh and Love wave maps provide information about the uppermost mantle, they should compare favorably with the P_n and S_n velocities seen in Fig. 9. Comparison is, in fact, very good in regions of good data coverage. The striking similarity of the high velocities of P_n and Rayleigh waves in northern Greenland is especially worth noting. Relatively low velocities across southern Greenland in comparison with velocities across the Canadian shield are in agreement with recent evidence from post-glacial rebound that southern Greenland has a thinner elastic lithosphere (J. Wahr, personal communication).

7. Conclusions

We have reported the results of a systematic study of surface wave dispersion, P_n, and S_n velocities across the Arctic region. The spatial resolution of the surface wave group velocity maps (300–500 km) is significantly higher than the resolution of global maps, particularly at the shorter periods, or maps obtained in previous regional studies. The resulting maps are robust to changes of damping parameters during the tomographic inversion and provide a very satisfactory fit to the observed dispersion curves.

The estimated isotropic group velocity maps clearly display the signatures of sedimentary and oceanic basins, crustal thickness variations, and upper mantle anomalies under both continents and oceans. They provide new constraints on the structure of sedimentary basins, the crust and upper mantle of the Arctic region. Comparison of the long-period group velocity maps with maps of P_n and S_n velocities demonstrates significant similarity in the pattern of the body and surface wave velocity distributions across the region in shield areas, along the tectonic belts of north-eastern Eurasia and north-western America, and along the Atlantic and Arctic MORs.

Preliminary maps of azimuthal anisotropy are encouraging in that they provide a consistent pattern of the orientation of fast directions both within our own data set and relative to the study of Trampert and Woodhouse (1996). This is especially true in the oceans. However, both the amplitudes and the patterns of anisotropy depend strongly on damping and further efforts are needed to determine which features of anisotropy are robust.

The next step in interpreting these results will be the joint inversion for a 3-D velocity model of the observed isotropic group velocity maps with the maps of P_n and S_n and, perhaps, phase velocity.

Acknowledgements

We would like to thank Jeannot Trampert for giving us his phase velocity azimuthal anisotropy model used in Figs. 10 and 11 and Bob Engdahl for providing the latest groomed ISC and NEIC data and consulting on the intelligent use of this data set. We are grateful to Stephanie Godey for her participation in the data

measurements of Rayleigh wave dispersion across North America. Most of data were acquired from the IRIS-DMC and Geoscope Data Centers. We would like to thank the staffs of these organizations for their assistance. We are also appreciative of the very helpful comments of Nikolai Shapiro, Florian Haslinger, and an anonymous reviewer. All maps were generated with the Generic Mapping Tools (GMT) data processing and display package (Wessel and Smith, 1991, 1995). This work was supported by NSF grant OPP-9818498 and partly by DSWA contract DSWA01-97-C-0157.

References

Barmin, M.P., Ritzwoller, M.H., Levshin, A.L., 2000. A fast and reliable method for surface wave tomography, Pure Appl. Geophys., in press.

Bijwaard, H., Spakman, W., Engdahl, E.R., 1998. Closing the gap between regional and global travel time tomography. J. Geophys. Res. 13, 30055–30078.

Calcagnille, G., Panza, G.F., 1978. Crust and upper mantle structure under the Baltic shield and Barents Sea from the dispersion of Rayleigh waves. Tectonophysics 47, 59–71.

Chan, W.W., Mitchell, B.J., 1985. Surface wave dispersion, crustal structure and sediment thickness variations across the Barents shelf. Geophys. J. R. Astr. Soc. 80, 329–344.

Chan, W.W., Mitchell, B.J., 1986. Regional variations in the crustal structure of northern Canada from surface wave dispersion. Geodynamics 6, 53–69.

Coles, R.L., Taylor, P.T., 1990. Magnetic anomalies. In: Grantz, A., Johnson, L., Sweeney, J.F. (Eds.), The Arctic Ocean Region, The Geology of North America. Boulder, CO, GSA, L, pp. 119–132.

Egorkin, A.A., Levshin, A.L., Yakobson, A.N., 1988. Study of the deep structure of the Barents Sea shelf by seismic surface waves. In: Numerical Modeling and Analysis of Geophysical Processes, Comput. Seismology, Vol. 20, Allerton Press, New York, pp. 197–201.

Engdahl, E.R., van der Hilst, R., Buland, R., 1998. Global teleseismic earthquake relocation with improved travel times and procedures for depth determination. Bull. Seismol. Soc. Am. 88, 722–743.

Ekström, G., Tromp, J., Larson, E.W.F., 1997. Measurements and global models of surface wave propagation. J. Geophys. Res. 102, 8137–8158.

Griot, D.A., Montagner, J.P., Tapponier, P., 1998. Surface wave phase velocity tomography and azimuthal anisotropy in Central Asia. J. Geophys. Res. 103, 21215–21232.

Hearn, T.M., Clayton, R.W., 1986. Lateral velocity variation in southern California, I. Bull. Seismol. Soc. Am. 76, 495–509.

Hearn, T., Beghoul, N., Barazangi, M., 1991. Tomography of the western United States from regional arrival times. J. Geophys. Res. 96, 16369–16381.

Hearn, T., Ni, J.F., 1994. P_n velocities beneath continental collision zones: the Turkish–Iranian plateau. Geophys. J. Int. 117, 273–283.

Johnson, L., Brass, G., 1998. Marine arctic science capability making big strides. EOS Trans. Am. Geophys. Un. 79, 345–349.

Kennett, B.L.N., Engdahl, E.R., Buland, R., 1995. Constraints on seismic velocities in the Earth from travel times. Geophys. J. Int. 122, 108–124.

Kijko, A., Mitchell, B.J., 1983. Multimode Rayleigh wave attenuation and Q in the crust of the Barents shelf. J. Geophys. Res. 88, 3315–3328.

Lander, A.V., Levshin, A.L., Ratnikova, L.I., Yakobson, A.N., 1985. Peculiarities of the deep structure of northern Eurasia from seismic surface wave data. In: Proceedings of the Academic Science, Vol. 285, No. 4. USSR, pp. 845–848 (in Russian).

Lander, A.V., 1989. Dispersion characteristics of Rayleigh waves on the Asiatic Arctic shelf and structural features of the Laptev Sea. In: Problems of Seismological Information Science, Comput. Seismology, Vol. 21, Allerton Press, New York, pp. 142–145.

Laske, G., Masters, G., 1997. A global digital map of sediment thickness, EOS Trans. AGU 78, F483.

Levshin, A.L., Berteussen, K.-A., 1979. Anomalous propagation of surface waves in the Barents Sea as inferred from NORSAR recordings. Geophys. J. R. Astr. Soc. 56, 97–118.

Levshin, A.L., Ratnikova, L.I., Berger, J., 1992. Peculiarities of surface wave propagation across the Central Eurasia. Bull. Seismol. Soc. Am. 82, 2464–2493.

Masters, G., Johnson, S., Laske, G., Bolton, H., 1996. A shear velocity model of the mantle. Phil. Trans. R. Soc. London A 354, 1385–1411.

Montagner, J.P., Tanimoto, T., 1991. Global upper mantle tomography of seismic velocities and anisotropies. J. Geophys. Res. 96, 20337–20351.

Mooney, W.D., Laske, G., Masters, G., 1998. CRUST5.1: a global model at 5 degrees by 5 degrees. J. Geophys. Res. 102, 727–748.

Ritzwoller, M.H., Levshin, A.L., 1998. Eurasian surface wave tomography: group velocities. J. Geophys. Res. 103, 4839–4878.

Ritzwoller, M.H., Levshin, A.L., Ratnikova, L.I., Egorkin, A.A., 1998. Intermediate period group velocity maps across Central Asia, Western China, and parts of the Middle East. Geophys. J. Int. 134, 315–328.

Ritzwoller, M.H., Barmin, M.P., Villaseñor, A., Levshin, A.L., Engdahl, E.R., 2000. P_n and S_n tomography across Eurasia, Tectonophysics, submitted for publication.

Rodi, W.L., Glover, P., Li, T.M.C., Alexander, S.S., 1975. A fast, accurate method for computing group-velocity partial derivatives for Rayleigh and Love modes. Bull. Seismol. Soc. Am. 65, 1105–1114.

Smith, M.L., Dahlen, F.A., 1973. The azimuthal dependence of Love and Rayleigh wave propagation in a slightly anisotropic medium. J. Geophys. Res. 78, 3321–3333.

Sobczak, L.W., Hearty, D.B., Forsberg, R., Kristoffersen, Y., Eldholm, O., May, S.D., 1990. Gravity from 64°N to the north pole. In: Grantz, A., Johnson, L., Sweeney, J.F. (Eds.), The Arctic Ocean Region, The Geology of North America. Boulder, CO, GSA, L, pp. 101–118.

Sultanov, D.D., Murphy, J.R., Rubinstein, Kh.D., 1999. A seismic source summary for Soviet peaceful nuclear explosions. Bull. Seismol. Soc. Am. 89, 640–647.

Trampert, J., Woodhouse, J., 1995. Global phase velocity maps of Love and Rayleigh waves between 40 and 150 s. Geophys. J. Int. 122, 675–690.

Trampert, J., Woodhouse, J., 1996. Global azimuthal anisotropy. Eur. Geophys. Soc. Newslet. 58, 57.

Van der Hilst, R.D., Widiyantoro, S., Engdahl, E.R., 1997. Evidence for deep mantle circulation from global tomography. Nature 386, 578–584.

Villaseñor, A., Ritzwoller, M.H., Levshin, A.L., Barmin, M.P., Engdahl, E.R., Spakman, W., Trampert, J., 2001. Shear velocity structure of central Eurasia from inversion of surface wave velocities.. Phys. Earth Planet. Int. 123, 169–184.

Wessel, P., Smith, W.H.F., 1991. Free software helps map and display data. Eos Trans. AGU 72, 441.

Wessel, P., Smith, W.H.F., 1995. New version of the generic mapping tools released. Eos Trans. AGU 76, 329.

Zeng, U., Teng, T.-L., Aki, K., 1989. Surface-wave mapping of the crust and upper mantle in the Arctic region. Bull. Seismol. Soc. Am. 79, 1520–1541.